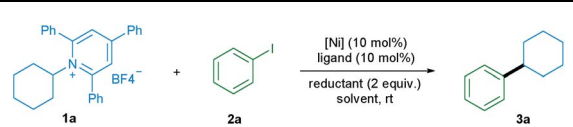


Table 1 Optimization of the reaction conditions^a


Entry	[Ni]	Ligand	Reductant	Solvent	Yield ^b (%)
1	NiCl ₂ ·dme	L1	Zn	DMA	29
2	NiCl ₂ ·dme	L1	Zn	DMF	11
3	NiCl ₂ ·dme	L1	Zn	CH ₃ CN	10
4	NiCl ₂ ·dme	L1	Zn	THF	16
5	NiCl ₂ ·dme	L1	Zn	Toluene	0
6 ^c	NiCl ₂ ·dme	L1	Zn	DMA	61
7 ^d	NiCl ₂ ·dme	L1	Zn	DMA	36
8 ^c	NiCl ₂ ·dme	L2	Zn	DMA	61
9 ^c	NiCl ₂ ·dme	L3	Zn	DMA	49
10 ^c	NiCl ₂ ·dme	L4	Zn	DMA	60
11 ^c	NiBr ₂ ·dme	L2	Zn	DMA	51
12 ^c	Ni(OAc) ₂ ·4H ₂ O	L2	Zn	DMA	15
13 ^c	Ni(acac) ₂	L2	Zn	DMA	35
14 ^c	NiCl ₂ ·6H ₂ O	L2	Zn	DMA	35
15 ^c	NiCl ₂ ·dme	L2	Mg	DMA	8
16 ^c	NiCl ₂ ·dme	L2	Mn	DMA	99
17 ^{c,e}	NiCl ₂ ·dme	L2	Mn	DMA	81
18 ^e	—	L2	Mn	DMA	0
19 ^e	NiCl ₂ ·dme	—	Mn	DMA	6
20 ^c	NiCl ₂ ·dme	L2	—	DMA	0



^a Reaction conditions: Katritzky pyridinium salt **1a** (0.1 mmol), iodobenzene **2a** (0.1 mmol), [Ni] (0.01 mmol), ligand (0.01 mmol), reductant (2 equiv.) in 1.0 ml solvent at rt. ^b GC yield using decane as the internal standard. ^c The ratio of **1a** to **2a** was set at 1.5 : 1. ^d The ratio of **1a** to **2a** was set at 1 : 2. ^e Bromobenzene was used instead of iodobenzene.

and **L4** showed a similar efficiency, providing the desired product in about 60% yield. With the readily available and cheap bipyridine **L2**, we examined a series of nickel catalysts, including NiBr₂·dme, Ni(OAc)₂·4H₂O, Ni(acac)₂, and NiCl₂·6H₂O. However lower yields were observed (entries 11–14). The yield was significantly improved to 99% when Mn powder was used as a reductant (entry 16), whereas the utilization of Mg powder gave the desired product in only 8% yield (entry 15). Besides aryl iodides, the protocol was also applied to aryl bromides. When bromobenzene was used, the desired product was also obtained in a good yield (entry 17). Control experiments demonstrated that the nickel catalyst, ligand, and reductant are all essential for the success of this transformation (entries 18–20).

With the optimized reaction conditions in hand, the scope of aryl halides was first evaluated (Table 2a). A wide variety of aryl halides bearing electron-donating, electron-neutral, and electron-withdrawing functional groups could be successfully converted into the corresponding products in good to excellent yields. For example, phenyl and biphenyl iodides and bromides

underwent this reaction smoothly, giving the corresponding products in excellent yields (**3a** and **3b**).

In addition, a wide range of functional groups including ketone (**3c** and **3d**), trifluoromethyl (**3e**), trifluoromethoxy (**3f**), trifluoromethylthio (**3g**), tosyl (**3h**), cyano (**3i** and **3m**), methoxy (**3j**), methylthio (**3k**), *t*-butyl (**3l**), fluoro (**3m**, **3r** and **5k**), and ester (**5j**) were well tolerated under the mild reaction conditions, highlighting the high chemoselectivity of this newly developed deaminative reductive cross-coupling reaction. Use of disubstituted aryl bromide and bicyclic substrates including phthalides and naphthyl halides also gave the products **3m–3p** in good yields. It is noteworthy that pharmaceutically relevant 3- and 4- bromopyridines could be applied to this protocol with good to high efficiency (**3q–3s**, **5n**). Next, the scope of pyridinium salts was explored. A wide range of structurally diverse pyridinium salts were suitable substrates for this transformation. Cyclic and acyclic secondary amine substrates could undergo this deaminative arylation reaction in good to excellent yield (**4a–4g**) and the same applies for *N*-heterocyclic pyridinium salts (**4h** and **4i**) (Table 2b).

It should be mentioned that when we applied primary alkyl pyridinium salts to this protocol, the reaction did not occur. However, simply switching the ligand from **L2** to **L4** and slightly raising the reaction temperature to 60 °C allowed this transformation to occur smoothly. A series of primary alkyl pyridinium salts bearing diverse functional groups such as amine, acetal, dioxole, cyclohexenyl, thiophene, and pyridine were suitable coupling partners for this deaminative reductive cross-coupling, leading to products **4n–4s**. Notably, chloro (**4k**), unprotected OH and indole NH groups were also tolerated (**4t** and **5f**), providing the option for further functionalization. Moreover, methylation reaction, which is challenging in reductive cross-coupling, was also realized *via* the utilization of methyl pyridinium salts (Table 2c). Importantly, our newly developed protocol could also be readily extended to a wide range of complex molecules derived from natural products and drugs. As such pregnenolone, galactopyranose, probenecid, adamantane carboxylic acid, and cholesterol derivatives could be transformed to the corresponding products **5a–5e** in good to excellent yield. Moreover, a series of pyridinium salts derived from drugs or drug intermediates, including tryptamine, mexitine, amphetamine, Lipitor intermediate, and dopamine, all underwent the mild coupling protocol with good to excellent efficiency (**5f–5n**). Use of Mosapride derived pyridinium salts gave product **5o** in a lower yield (Table 2d).

Additionally, a gram-scale reaction was successfully conducted using **1a** and 4-iodobiphenyl **2b** in the presence of only 5 mol% nickel catalyst and the desired product **3b** was obtained in 96% yield (Scheme 2a), demonstrating the practicability of our newly developed deaminative reductive cross-coupling methodology. Also, byproduct **6**, which is potentially a useful organic base, could be isolated in 85% yield. To shed light on the mechanism of this transformation, an experiment was conducted with the radical trapping reagent TEMPO (2,2,6,6-tetramethyl-1-piperidinyloxy, 2 equiv.).^{5a,c} The reaction was suppressed and no product **5m** was detected (Scheme 2b).

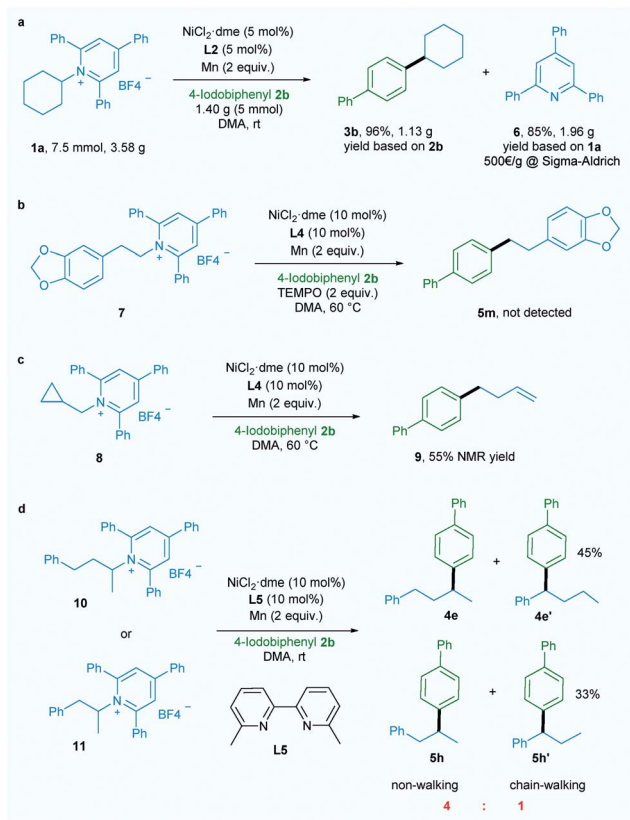


Table 2 Scope of substrates^a

^a Reaction conditions: pyridinium salt **1** (0.30 mmol), aryl halide **2** (0.20 mmol), NiCl₂·dme (0.02 mmol), **L2** (0.02 mmol, for secondary alkyl) or **L4** (0.02 mmol, for primary alkyl), Mn powder (0.40 mmol) in 1.0 ml DMA at rt (for secondary alkyl) or 60 °C (for primary alkyl); yields after purification.

^b GC yield. ^c The ratio of pyridinium salt to aryl halide 1 : 3, 100 °C, NMR yield.

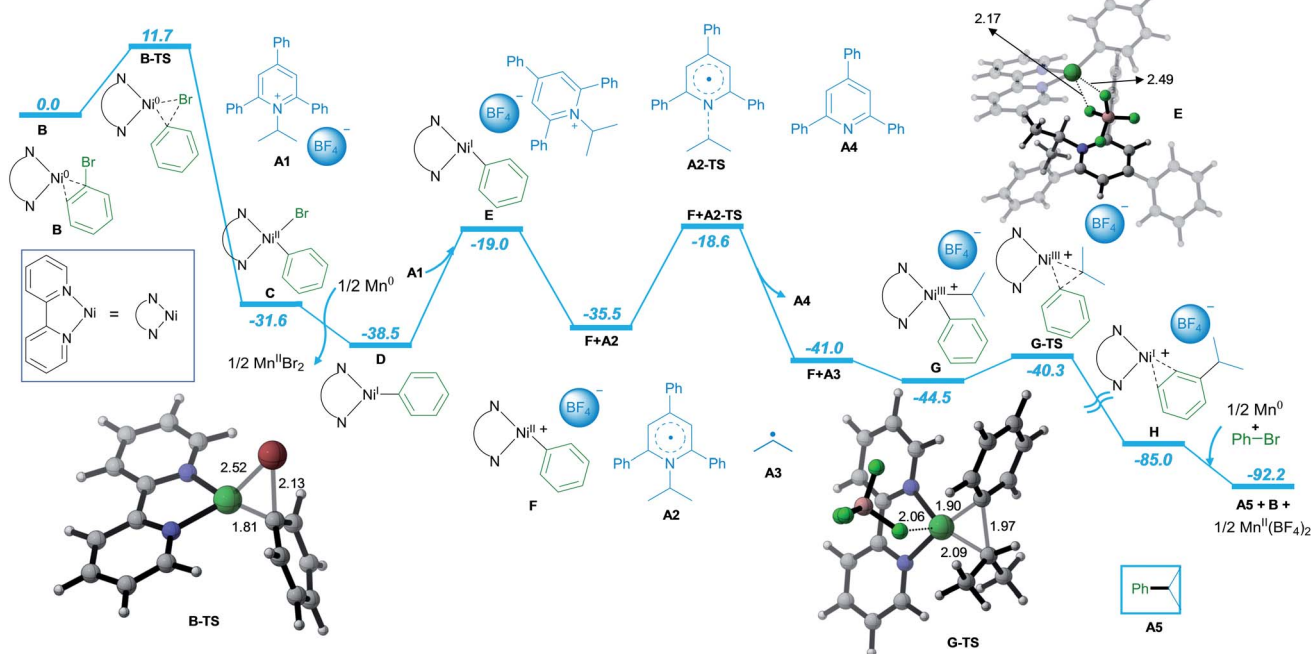




Scheme 2 Gram-scale reaction and mechanism investigation.

Also, ring-opened product **9** was generated in 55% yield when a substrate bearing a cyclopropane motif **8** was used (Scheme 2c).^{5a,c} Both these results suggest the involvement of an alkyl radical in this transformation. When ligand **L5** which is effective for chain-walking reductive cross-coupling¹⁰ was used in our catalytic system, non-walking and chain-walking products (**4e** and **4e'**, **5h** and **5h'**) were obtained with a ratio of 4 : 1, suggesting an oxidative addition of aryl halide to Ni⁰ to give a Ni^{II} intermediate prior to alkyl radical generation. Since the Ni^{III} intermediate generated from addition of the alkyl radical to the Ni^{II} intermediate is less likely to undergo the chain-walking step due to steric hindrance the non-chain-walking product is the major product.

Furthermore, detailed DFT calculations were performed to rationalize our newly designed catalytic reaction (Scheme 3; computational methods, see ESI[†]). As a model system, we investigated the reaction of phenyl bromide with **A1** in the presence of NiCl₂·dme, bpy as the ligand and Mn as the reducing agent. The reaction starts with the complexation of the ligand bpy to the Ni^{II} precatalyst, followed by reduction to form the active Ni⁰ catalyst **B** (Scheme S1 in ESI[†]). The catalytic process is initiated by oxidative addition of phenyl bromide to Ni⁰ *via* transition state **B-TS** with an energy barrier of 11.7 kcal mol⁻¹. The formed Ni^{II} intermediate **C** is reduced by Mn, leading to intermediate **D** with a free energy gain of 6.9 kcal mol⁻¹. In the next step, **A1** is coordinated to **D**, followed by SET reduction of **A1** to generate radical **A2** and Ni^{II} intermediate **F**. The radical **A2** is prone to undergo C–N bond cleavage with an energy barrier of 19.9 kcal mol⁻¹, liberating the alkyl radical **A3** and the aromatic pyridine **A4**. At this point, alkyl



Scheme 3 DFT-Computed energy profile for the nickel-catalyzed reductive cross-coupling reaction of aryl halides and pyridinium salts. Free energies in solution (in kcal mol⁻¹) at the SMD(DMA)-M06/Def2-QZVPP//ωB97xD/Def2-TZVP(Ni,Mn)/Def2-SVP (non-metal) level are displayed. Selected DFT optimized geometries are listed. Bond lengths are in Å.



radical **A3** adds to Ni^{II} intermediate **F** to form Ni^{III} intermediate **G**. Subsequently, the C–C bond cross-coupling product **A5** is formed *via* reductive elimination from Ni^{III} with an energy barrier of 4.9 kcal mol⁻¹.

Finally, the Ni^I intermediate **H** is further reduced by Mn to regenerate the Ni⁰ active catalyst **B** and initiate the next catalytic cycle.

Subsequently, we focused on the origin of the SET reduction of the pyridinium salt and the generation of the alkyl radical.¹¹ The molecular orbital plots (Fig. 1a) show that the SOMO of **E** corresponds to the singly occupied MO predominantly localized on the d_{z²}-orbital of Ni. At the same time, the LUMO of **E** corresponds to a π-orbital delocalized around the central nitrogen-containing aromatic ring of the pyridinium salt. However, after **A2** is displaced away from the Ni species, the SOMO becomes localized on the central aromatic ring of the pyridinium salt. This indicates that upon separation of the Ni and pyridyl fragments the unpaired electron transfers from Ni to the pyridinium salt and delocalizes around the central aromatic ring. Spin density analysis further supported this process. The unpaired electron density is localized on the Ni-center when the pyridinium salt is coordinated to the Ni^I-complex, as in **E** (Fig. 1b, left), while it is transferred to the central pyridine ring as the pyridine moiety **A2** dissociates from the Ni complex (Fig. 1b, middle). Subsequently, the C–N bond dissociates and the spin density is further transferred to the sp³-carbon atom, indicating generation of the alkyl radical (Fig. 1b, right). Additionally, cyclic voltammetry (CV) measurements of

the pyridinium salt were conducted (see ESI†) and reversible peaks at -0.94 V *vs.* SCE were observed, suggesting the existence of stable radical intermediate **A2**. In order to understand the C–N bond dissociation, we performed localized orbital locator (LOL) – π analysis¹² and multi-center bond order calculations (I_{ring})¹³ for the whole process (Fig. 1c). Before the SET reduction, the central pyridine ring has full aromaticity ($I_{\text{ring}} = 0.05$ in **A1**, for comparison, $I_{\text{ring}} = 0.05$ in benzene and pyridine^{12c}). After the reduction the aromaticity is lost and the free energy is 3.0 kcal mol⁻¹ higher ($I_{\text{ring}} = 0$ in **A2**). With the C–N bond dissociating, the aromaticity is partially regained (*c.f.* $I_{\text{ring}} = 0.01$ in transition state **A2TS**). After the generation of alkyl radicals, the aromaticity of **A3** is fully restored ($I_{\text{ring}} = 0.05$ in **A3**) with a free energy gain of 5.5 kcal mol⁻¹.

3. Conclusions

In summary, we have developed a new deaminative reductive cross-coupling of aryl halides with pyridinium salts derived from readily available alkyl amines. Due to the avoidance of stoichiometric organometallic reagents and external bases, the scope is rather broad as demonstrated using the many different substrates employed (>55 examples). In addition, the chemoselectivity of this protocol is good and functional groups, including cyano, methoxy, methylthio, fluoro as well as chloro, unprotected OH and indole NH groups, are well tolerated. Importantly, the cross-coupling reaction can be scaled-up using a lower amount of nickel catalyst without diminishing the yield, demonstrating the practicability of this protocol. Furthermore, experimental mechanistic investigations and DFT calculations combined with wavefunction analysis have been conducted to gain insight into the catalytic process.

Conflicts of interest

There are no conflicts to declare.

Acknowledgements

H. Y. acknowledges the China Scholarship Council. C. Z. acknowledges the King Abdullah University of Science and Technology (KAUST) for support and the KAUST Supercomputing Laboratory for providing computational resources of the supercomputer Shaheen II.

Notes and references

- (a) T. J. Colacot, *New Trends in Cross-Coupling: Theory and Applications*, RSC Publishing, Cambridge, 2014; (b) A. d. Meijere, S. Bräse and M. Oestreich, *Metal-Catalyzed Cross-Coupling Reactions and More*, Wiley-VCH, Weinheim, 2014.
- (a) C. E. Knappke, S. Grupe, D. Gärtner, M. Corpet, C. Gosmini and A. Jacobi von Wangelin, *Chem.–Eur. J.*, 2014, **20**, 6828–6842; (b) J. Gu, X. Wang, W. Xue and H. Gong, *Org. Chem. Front.*, 2015, **2**, 1411–1421; (c) D. J. Weix, *Acc. Chem. Res.*, 2015, **48**, 1767–1775.



Fig. 1 (a) Molecular orbital plots: SOMO of **E** (left), LUMO of **E** (middle) and SOMO of **Eb** (right). (b) Spin density plots of **E** (left), **Eb** (middle) and **A2TS** (right). (c) Localized orbital locator (LOL) – π plots of **A1**, **A2**, **A2TS**, and **A3** with multi-center bond order of the central nitrogen-containing aromatic ring I_{ring} listed below.



- 3 D. A. Everson, R. Shrestha and D. J. Weix, *J. Am. Chem. Soc.*, 2010, **132**, 920–921.
- 4 Examples of reductive cross couplings with N-hydroxyphthalimide esters: (a) K. M. Huihui, J. A. Caputo, Z. Melchor, A. M. Olivares, A. M. Spiewak, K. A. Johnson, T. A. DiBenedetto, S. Kim, L. K. G. Ackerman and D. J. Weix, *J. Am. Chem. Soc.*, 2016, **138**, 5016–5019; (b) L. Huang, A. M. Olivares and D. J. Weix, *Angew. Chem., Int. Ed.*, 2017, **56**, 11901–11905; (c) N. Suzuki, J. L. Hofstra, K. E. Poremba and S. E. Reisman, *Org. Lett.*, 2017, **19**, 2150–2153; (d) H. Li, C. P. Breen, H. Seo, T. F. Jamison, Y.-Q. Fang and M. M. Bio, *Org. Lett.*, 2018, **20**, 1338–1341; (e) X. Lu, X.-X. Wang, T.-J. Gong, J.-J. Pi, S.-J. He and Y. Fu, *Chem. Sci.*, 2019, **10**, 809–814; anhydrides: (f) H. Chen, L. Hu, W. Ji, L. Yao and X. Liao, *ACS Catal.*, 2018, **8**, 10479–10485; benzyl oxalates: (g) X.-B. Yan, C.-L. Li, W.-J. Jin, P. Guo and X.-Z. Shu, *Chem. Sci.*, 2018, **9**, 4529–4534; tosylates and mesylates: (h) J. H. Liu, C. T. Yang, X. Y. Lu, Z. Q. Zhang, L. Xu, M. Cui, X. Lu, B. Xiao, Y. Fu and L. Liu, *Chem.–Eur. J.*, 2014, **20**, 15334–15338.
- 5 For leading work, see: (a) C. H. Basch, J. Liao, J. Xu, J. J. Piane and M. P. Watson, *J. Am. Chem. Soc.*, 2017, **139**, 5313–5316; (b) J. Liao, W. Guan, B. P. Boscoe, J. W. Tucker, J. W. Tomlin, M. R. Garnsey and M. P. Watson, *Org. Lett.*, 2018, **20**, 3030–3033; (c) S. Plunkett, C. H. Basch, S. O. Santana and M. P. Watson, *J. Am. Chem. Soc.*, 2019, **141**, 2257–2262.
- 6 (a) F. J. Klauck, M. J. James and F. Glorius, *Angew. Chem., Int. Ed.*, 2017, **56**, 12336–12339; (b) X. Jiang, M.-M. Zhang, W. Xiong, L.-Q. Lu and W.-J. Xiao, *Angew. Chem., Int. Ed.*, 2019, **58**, 2402–2406; (c) F. J. Klauck, H. Yoon, M. J. James, M. Lautens and F. Glorius, *ACS Catal.*, 2018, **9**, 236–241; (d) M. Ociepa, J. Turkowska and D. Gryko, *ACS Catal.*, 2018, **8**, 11362–11367.
- 7 (a) J. Wu, L. He, A. Noble and V. K. Aggarwal, *J. Am. Chem. Soc.*, 2018, **140**, 10700–10704; (b) F. Sandfort, F. Strieth-Kalthoff, F. J. Klauck, M. J. James and F. Glorius, *Chem.–Eur. J.*, 2018, **24**, 17210–17214.
- 8 J. Hu, G. Wang, S. Li and Z. Shi, *Angew. Chem., Int. Ed.*, 2018, **57**, 15227–15231.
- 9 Examples: (a) M. Leiendecker, C. C. Hsiao, L. Guo, N. Alandini and M. Rueping, *Angew. Chem., Int. Ed.*, 2014, **53**, 12912–12915; (b) L. Guo, A. Chatupheeraphat and M. Rueping, *Angew. Chem., Int. Ed.*, 2016, **55**, 11810–11813; (c) L. Guo, C.-C. Hsiao, H. Yue, X. Liu and M. Rueping, *ACS Catal.*, 2016, **6**, 4438–4442; (d) L. Guo, X. Liu, C. Baumann and M. Rueping, *Angew. Chem., Int. Ed.*, 2016, **55**, 15415–15419; (e) X. Liu, C. C. Hsiao, I. Kalvet, M. Leiendecker, L. Guo, F. Schoenebeck and M. Rueping, *Angew. Chem., Int. Ed.*, 2016, **55**, 6093–6098; (f) H. Yue, L. Guo, S. C. Lee, X. Liu and M. Rueping, *Angew. Chem., Int. Ed.*, 2017, **56**, 3972–3976; (g) H. Yue, L. Guo, H. H. Liao, Y. Cai, C. Zhu and M. Rueping, *Angew. Chem., Int. Ed.*, 2017, **56**, 4282–4285; (h) H. Yue, C. Zhu and M. Rueping, *Angew. Chem., Int. Ed.*, 2018, **57**, 1371–1375.
- 10 F. Chen, K. Chen, Y. Zhang, Y. He, Y.-M. Wang and S. Zhu, *J. Am. Chem. Soc.*, 2017, **139**, 13929–13935.
- 11 (a) Molecular orbital plot, spin density plot, and LOL- π plot were visualized by VMD, see: W. Humphrey, A. Dalke and K. Schulten, *J. Mol. Graphics*, 1996, **14**, 33–38; (b) Molecular orbitals, spin density, LOL- π , and multi-center bond order were analyzed by Multiwfn 3.6. see: T. Lu and F. Chen, *J. Comput. Chem.*, 2012, **33**, 580–592.
- 12 (a) H. Schmider and A. Becke, *J. Mol. Struct.: THEOCHEM*, 2000, **527**, 51–61; (b) V. Tsirelson and A. Stash, *Acta Crystallogr., Sect. B: Struct. Sci.*, 2002, **58**, 780–785; (c) H. Jacobsen, *Can. J. Chem.*, 2008, **86**, 695–702.
- 13 (a) M. Giambiagi, M. S. de Giambiagi and K. C. Mundim, *Struct. Chem.*, 1990, **1**, 423–427; (b) P. Bultinck, R. Ponc and S. Van Damme, *J. Phys. Org. Chem.*, 2005, **18**, 706–718; (c) E. Matito, *Phys. Chem. Chem. Phys.*, 2016, **18**, 11839–11846.

